



1

2 **Mauro Guglielmin<sup>1\*</sup>, Marco Donatelli<sup>2</sup>, Matteo Semplice<sup>3</sup>, Stefano Serra Capizzano<sup>2,4</sup>.**

3

4

5 <sup>1</sup> Department of Theoretical and Applied Sciences, Insubria University, Via Dunant 3, 21100 Varese <sup>2</sup>  
6 Department of Science and High Technology, Insubria University; <sup>3</sup> Department of Mathematics, University of  
7 Turin; <sup>4</sup> Department of Information Technology, Uppsala University.

8

\* Correspondence to Mauro Guglielmin: [mauro.guglielmin@uninsubria.it](mailto:mauro.guglielmin@uninsubria.it);

9

10

11

12 **Ground surface temperature reconstruction for the last 500 years obtained from**  
13 **permafrost temperatures observed in the Stelvio Share borehole, Italian Alps.**

14

## 15 **ABSTRACT**

16 The general pattern of ground surface temperatures (GST) reconstructed from the permafrost Stelvio Share  
17 Borehole (SSB) for the last 500 years are similar to the mean annual air temperature (MAAT) reconstructions  
18 for the European Alps. The main difference with respect to MAAT reconstructions relates to post Little Ice Age  
19 (LIA) events. Between 1940 and 1989, SSB data indicate a 0.9°C cooling. Subsequently, a rapid and abrupt GST  
20 warming (more than 0.8°C per decade) was recorded between 1990 and 2011. This warming is of the same  
21 magnitude as the increase of MAAT between 1990 and 2000 recorded in central Europe and roughly double the  
22 MAAT in the Alps.

23

24

25

26

27



28

29

## 30 **1 INTRODUCTION**

31 The thermal regime of the uppermost ground is determined by the geothermal heat flow and by the  
32 fluctuations of temperature at the surface. If rock was homogeneous and no temperature change were to  
33 occur at the surface, the temperature would increase linearly with depth. The gradient of this temperature  
34 increase would be governed solely by the magnitude of the terrestrial heat flow and by the thermal  
35 conductivity of the rock. However, variations of ground surface temperature (GST) propagate downwards into  
36 the rock as attenuating thermal waves, superimposed on the aforementioned linear temperature profile. The  
37 depth to which disturbances can be recorded is determined mainly by the amplitude and duration of the  
38 temperature change at the surface. Generally, propagation of climate signals is slow and it can take more than  
39 1,000 years to reach the depth of 500m (Huang et al., 2000). For a better conservation of the climate signal in  
40 the thermal profile, no lateral heat advection (due for example to ground water flow) should be present (Lewis  
41 and Wang, 1992). Since normally no groundwater circulation is present within permafrost, boreholes drilled  
42 into it are particularly suited for GST reconstructions.

43 Lachenbruch and Marshall (1986) were among the first to demonstrate that thermal profiles obtained from  
44 boreholes drilled in permafrost can be used to reconstruct ground surface temperature changes. These do not  
45 require calibration because the heat conduction equation is directly used to infer temperature changes at the  
46 ground surface. Today, the majority of permafrost boreholes used to reconstruct ground surface temperatures  
47 are located in the Polar regions of North America and Eurasia where the boreholes can be drilled on flat terrain,  
48 with negligible topographical effects, and with a permafrost thicknesses typically exceed 100 m, thereby  
49 providing deep temperature logs and long ground surface temperature reconstructions.

50 The Share Stelvio borehole (SSB) in the Italian Alps is the deepest drilled within permafrost in the mid-latitude  
51 mountains of Europe. Because the permafrost thickness exceeds 200 m at this site, it allows reconstruction of  
52 the ground surface temperature for much of the last millennium. In addition, the Stelvio borehole is located on  
53 a rounded summit with gentle side slopes. Therefore, site-specific topographic influences are largely eliminated.  
54 As such, it is different to the other boreholes drilled in permafrost in the Alps (e.g. PACE boreholes at Schilthorn  
55 or Stockhorn; see Harris et al., 2003; Gruber et al., 2004; Hilbich et al., 2008; Harris et al., 2009).

56 Recent atmospheric warming (over the last century) in the European Alps has been roughly twice the global  
57 average (Böhm et al., 2001; Auer et al., 2007). Despite its high sensitivity, no GST reconstruction based on  
58 borehole thermal profiles is available for this part of the world. Instead, reconstructions of summer air  
59 temperatures have been based on either tree-rings (e.g. Büntgen et al., 2006; Corona et al., 2010) or lake  
60 sediments (e.g. Larocque-Tobler et al., 2010; Trachsel et al., 2010) for the last 500-1000 years, or both (Trachsel  
61 et al., 2012). With rare exceptions (e.g. ice cores; Barbante et al., 2004), the other proxy data are from sites at  
62 elevations that rarely exceed 2000m a.s.l. and all the other monitored permafrost boreholes in Europe do not  
63 exceed 100 m of depth (see Harris et al., 2003). However, several papers describe GST reconstructions for the



64 last 500-1000 years using boreholes data at hemispheric or global scales (e.g. Huang et al., 2000; Beltrami and  
65 Boulron, 2004).

66 The SSB data provides GST history from a high elevation site (3000 m a.s.l.). Such locations are important  
67 because snow cover can affect significantly the GST (Zhang, 2005; Ling and Zhang, 2006; Cook et al., 2008). They  
68 are also relevant with respect to glacier dynamics and their feedbacks with the global atmospheric system  
69 (IPCC, 2013).

70 This paper reconstructs the ground surface temperatures inferred from this borehole and compares the results  
71 with existing multiproxy reconstructions for the European Alps and elsewhere.

72

## 73 **2 STUDY AREA**

74 The Stelvio–Livrio area is a summer ski location, located between the Stelvio Pass (2758 m a.s.l.) and Mt Livrio  
75 (3174 m a.s.l.), within the Stelvio National Park. The area is characterized by bedrock outcrops (mainly  
76 dolostone), apart from some Holocene moraines (Figure 1a). The SSB borehole was drilled in 2009 and is only  
77 10m from the PACE borehole, drilled in 1998 (46°30'59"N; 10°28'35"E, 3000 m a.s.l., Figure 1b). Both boreholes  
78 are located on a flat barren summit surface oriented NNW-SSE. The side slopes (SSW and NNE exposed) are  
79 gentle, the northern being only slightly steeper (14.1° vs 12.5° vs from the top down to 2900 m a.s.l.; Fig. 2).  
80 Despite their closeness, the two boreholes differ in ice content: during drilling of the PACE borehole ice were  
81 encountered at 42 and 90 m depth (Guglielmin et al., 2001) but no evidence of ice was observed during the SSB  
82 drilling. Using PACE temperature profile and typical thermal conductivity and heat flow values cited in literature  
83 ( $4.0 \text{ W}^{-1}\text{K}^{-1}$ , Clauser and Huenges, 1995;  $85 \text{ mW m}^{-2}$ , Cermak et al., 1992), permafrost thickness in the SSSB  
84 borehole was estimated to be around 220 m.

85

86

## 87 **3 METHODS**

### 88 **3.1 Field data**

89 The SSB borehole was drilled in early July, 2010, using refrigerated compressed-air-flush drilling technology. The  
90 stratigraphy was obtained by analyses of the cuttings (sampled every 10 m) and, for the first 100 m, through  
91 analysis of TV logging. Since September 2010, the thermal regime of the SSB borehole was monitored with  
92 thermometers placed according to the PACE protocol (Harris et al., 2001). The accuracy of the thermometers is  
93  $0.1^\circ\text{C}$  and the resolution is  $0.01^\circ\text{C}$ . Since 1998, the main climatic parameters at the site (air temperature, snow  
94 cover, incoming radiation) have been monitored. Below the 20m depth, no significant seasonal variations in  
95 temperature are recorded.



### 96 **3.2 Laboratory data**

97 The thermal properties of the three main facies observed in the stratigraphy were measured in the laboratory  
98 at three different temperatures (0°C, -1°C; -3°C). Thermal diffusivity and specific heat were measured by  
99 NETZSCH Gerätebau GmbH (Selb, Germany) using a NETZSCH model 457 MicroFlash™ laser flash diffusivity  
100 apparatus. Thermal diffusivity measurements were conducted in a dynamic helium atmosphere at a flow rate of  
101 c. 100 ml/min between -3 °C and 0 °C. Specific heat capacity was measured using the ratio method of ASTM-E  
102 1461 (ASTM, 2003) with an accuracy of more than 5%. Density of the rock at room temperature was  
103 determined using the buoyancy flotation method with an accuracy better than 5%. Thermal conductivity was  
104 calculated following Carslaw and Jaeger (1959):

$$105 \quad \lambda = \rho * c_p * \kappa,$$

106 where  $\lambda$  is the thermal conductivity ( $\text{W m}^{-1} \text{K}^{-1}$ ),  $\rho$  is the bulk density ( $\text{gcm}^{-3}$ ),  $c_p$  is the specific heat capacity  
107 ( $\text{Jg}^{-1} \text{K}^{-1}$ ), and  $\kappa$  is the thermal diffusivity ( $\text{m}^2 \text{s}^{-1}$ ).

### 108 **3.3 Theory**

109 The temperature anomaly in the borehole at time  $t$  at depth  $z$  is modeled by the solution of the heat equation

$$110 \quad \frac{\partial A}{\partial t} - \frac{\partial}{\partial z} \left( \kappa \frac{\partial A}{\partial z} \right) = 0 \quad (1)$$

111 for the domain  $(t, z) \in (-t_{\max}, 0) \times (0, z_{\max})$ . Note that equation (1) can be derived from the classical  
112 formulation of Carslaw and Jaeger (1959) under the hypothesis that the density and the specific heat capacity  
113 are constant with respect to the depth  $z$  (see also Liu and Zhang, 2014), which is a good approximation for the  
114 SSB (see Section 4.1). Further, we have indicated with  $t_{\max}$  the earliest time for which we will reconstruct the  
115 GST and with  $z_{\max}$  the depth of the borehole. Equation (1) can be solved to compute the temperature anomaly  
116 at any given past time  $t$  and depth  $z$  from the boundary values  $A(t; 0)$  which represent the GST history. In our  
117 case instead, we need to solve the inverse problem of finding the GST from the borehole data, which provide  
118 the anomaly measured at present ( $t=0$ ) or past times ( $t>0$ ) at some depth  $z$  in the borehole. If the boundary  
119 data  $A(t,0)$  is piece-wise constant, the solution of the direct problem for equation (1) can be found explicitly  
120 (see Carslaw and Jaeger, 1959). In fact, the anomaly observed in the borehole  $t$  years ago, originating from a  
121 GST that has been constant except for an increase of  $\delta$  °C between  $t_2$  and  $t_1$  years ago is:

$$122 \quad A(t, z) = \delta \left[ \operatorname{erfc} \left( \frac{z}{\sqrt{4\kappa(t_2 - t)}} \right) - \operatorname{erfc} \left( \frac{z}{\sqrt{4\kappa(t_1 - t)}} \right) \right]$$

123 The above formula of course makes sense only for  $t < t_1$  and the value  $t = 0$  corresponds to present time. For  
124 the purpose of reconstructing the GST history, it is customary to approximate it with a piece-wise constant  
function (see Figure 3)



125

$$\text{GST}(t) = \begin{cases} \tau_k, & t \in [-t_k, -t_{k-1}] \\ \tau_\infty, & t < -t_N \end{cases} \quad (2)$$

126 where  $t_k$ , for  $k = 1, \dots, N$ , is the sequence of times in the past where we want to compute the value of the GST,  
 127 and the  $\tau_k$ 's are the unknown values to be computed. The prediction of model (1) for the borehole temperature  
 128  $t$  years ago, originating from the GST (2) is

$$A(z, t) = \tau_1 \varphi(z, t_1 - t) + \sum_{k=1}^N \tau_k [\varphi(z, t_{k+1} - t) - \varphi(z, t_k - t)] - \tau_\infty \varphi(z, t_N - t), \quad (3)$$

129 where  $\varphi(z, t) = \text{erfc}\left(\frac{z}{\sqrt{4kt}}\right)$ . Once the sequence  $t_k$  is chosen, the relation between the borehole temperature at  
 130 depth  $z_j$  predicted by the model and the unknown values  $\tau_k$  of the GST anomaly is thus linear. When  
 131 comparing the anomaly  $A(z, t)$  described by the above equation with the measured data in the borehole, one  
 132 has to take into account that measured data represent the superposition of the anomaly with a background  
 133 signal (linearly increasing with depth) coming from the heat flow. This linear trend can be identified by linearly  
 134 fitting the data from the deepest part of the borehole (below 60m in our case). Following (3), imposing that the  
 135 borehole temperatures measured  $T_j$  years ago at depth  $z_j$  leads to the linear system

$$L\vec{\tau} = \vec{m}, \quad (4)$$

136 where the column vector  $\vec{\tau} = [\tau_1, \tau_2, \dots, \tau_N, \tau_\infty]$  collects the unknown GST values,  $\vec{m}$  is the column vector of  
 137 detrended measured data and  $L$  is a matrix with  $M \times (J + 1)$  entries given by

$$\begin{aligned} L_{j,1} &= \varphi(Z_j, t_1 - T_j) \\ L_{j,k} &= \varphi(Z_j, t_{k+1} - T_j) - \varphi(Z_j, t_k - T_j) \\ L_{j,N+1} &= \varphi(Z_j, t_N - T_j). \end{aligned}$$

138 The diffusive nature of the heat equation has the effect that fine details of GST signals are averaged away as  
 139 time progresses. Therefore, in the field data, one can find signals coming only from long wavelength GST  
 140 variations occurred in the distant past, whereas short wavelength signals are observable only if produced in the  
 141 more recent history. Our first task is to choose the length of the GST reconstruction ( $t_N$ ) and the reconstruction  
 142 points between the present and  $t_N$ . In order to take into account long and short wavelengths variations of GST  
 143 where each of them makes sense, contrary to the common use of choosing uniformly spaced time points, we  
 144 choose

$$t_k = (1 + 0.2k)^2$$

145 so that the reconstruction points are closer to each other in the recent past and more separated for distant  
 146 ages. The choice of the parameter 0.2 is such that the reconstructed GST can contain signals of wavelength of at  
 147 least 33 years from 1600 onwards, 23 years from 1800 onwards, 16 years from 1915 onwards, 9 years from  
 148 1985 onwards.



149 We point out that the explicit inclusion in (3) of the time  $t$  at which the temperature was measured allows us to  
 150 gather in the single linear system (4) with data measured at different times. In fact each row of the matrix  $L$  can  
 151 have a different value of  $T_j$ . In this fashion, the GST reconstruction can be based not only on a single  
 152 temperature profile but also on the variation of the temperature profile between the present and some years  
 153 ago. To the best of our knowledge, this possibility, which enhances the robustness of the reconstruction, has  
 154 never been exploited before in the literature. Given the detrended measures  $\vec{m}$ , we must compute the vector  $\vec{\tau}$   
 155 solving the linear system (4). Since the inverse problem for the heat equation (1) is well-known to be severely  
 156 ill-posed, the matrix  $L$  is strongly ill-conditioned and its singular values decay exponentially to zero, with related  
 157 singular vectors largely intersecting the subspace of high frequencies (Serra-Capizzano, 2004). Therefore, since  
 158 the right-hand side  $\vec{m}$  is affected by error measurements, solving directly the linear system (4) would lead to a  
 159 computed GST that would be highly oscillating and very far from the true physical values for  $\vec{\tau}$ . It is then  
 160 necessary to introduce a regularization process by modifying the original problem (4), in order to obtain an  
 161 approximation that is well posed and less sensitive to errors in the right-hand-side of (4). Classical regularization  
 162 techniques include the truncated singular value decomposition (TSVD) and the Tikhonov regularization in  
 163 standard form (Hansen, 1998), applied in Beltrami and Boulron, (2004) and Liu and Zhang, (2014), respectively.  
 164 The Tikhonov regularization usually provides better restorations than the TSVD, because it is characterized by a  
 165 smooth transition in the filtering of the frequencies and the smoothness of the transition can be somehow  
 166 chosen by manipulating the regularization parameter of the method (Hansen, 1998). In this paper, we thus  
 167 propose the use of the generalized Tikhonov regularization, where the damping term is measured by a proper  
 168 seminorm. In practice, instead of dealing with the linear system (4), we solve the minimization problem

$$\min_{\vec{\tau}} \|L\vec{\tau} - \vec{m}\| + \alpha \|R\vec{\tau}\| \quad (5)$$

169 where  $\alpha > 0$  is the regularization parameter and  $R$  is the regularization matrix. When  $\alpha$  is large the restored  
 170 GST is very smooth but the differences between the measured data and the temperatures in the well that  
 171 would be computed by (4) from the recovered GST are large. On the contrary, when  $\alpha$  is too small the data  
 172 fitting is good but the GST becomes highly oscillating due to the ill-posedness. A good tradeoff is not trivial and  
 173 several strategies can be explored for estimating an optimal value of  $\alpha$ : as an example, the generalized cross  
 174 validation (Golub et al., 1979) often provides good results. The use of a regularization matrix  $R$  for this  
 175 application is a novelty introduced in this paper. If  $R$  is simply the identity matrix, then the problem (5) reduces  
 176 to the standard Tikhonov method used in Liu and Zhang, (2014). The presence of the matrix  $R$  in (5) allows to  
 177 impose some a-priori information on the true solution. Indeed, when minimizing (5), the components of the  
 178 solution belonging to  $\ker(R) = \{\vec{x} \text{ s.t. } R\vec{x} = \vec{0}\}$  (the kernel of matrix  $R$ ) are not damped and are therefore  
 179 perfectly reconstructed. Note that in order to guarantee the uniqueness of the solution (5), the condition  
 180  $\ker(L) \cap \ker(R) = \vec{0}$  has to hold.

181 A common choice for  $R$  is a finite difference discretization of a differential operator (Hansen, 1998]. In this  
 182 paper, we consider a standard discretization of the Laplacian

183



184

185

186

187

$$R = \begin{bmatrix} -1 & 2 & -1 & & & \\ & -1 & 2 & -1 & & \\ & & \ddots & \ddots & \ddots & \\ & & & -1 & 2 & -1 \end{bmatrix}$$

188 of size  $(N - 2) \times N$  and hence the constant and linear components of the solution are not damped in the  
189 Tikhonov regularization (5).

190

## 191 4 RESULTS

### 192 4.1 Permafrost temperature, thermal properties and GST reconstruction

193 The SSB stratigraphy is characterized by four different facies of dolostone (Figure 4): a massive dolostone (from  
194 grey to pinky grey) comprises more than 90% of the profile; three other facies (white dolostone, black stratified  
195 limestone, brownish dolostone) are thin intercalations (maximum 3.5 meters of thickness and located mainly in  
196 the first 42 m).

197 The mean annual thermal profiles of the last three years (2013-14-15) show a negative gradient between 20 m  
198 (a depth corresponding approximately to the depth of zero annual amplitude, ZAA) and 60 m that does not vary  
199 ( $-0.8^{\circ}\text{C}/100$  m in all the three years). At greater depth, the gradient is positive with slightly different slopes  
200 between 60-105; 105-125; 125-205; 205-215 and 215-235 (Figure 5 and Table 1).

201 Table 2 shows the thermal properties of the three main stratigraphic facies encountered in the borehole. Facies  
202 a and c show similar density and thermal properties while facies b has higher density and higher conductivity.  
203 All facies have heat capacity values that increase with a decrease of temperature. In facies a, this behavior  
204 occurs also for thermal conductivity and diffusivity values. In contrast, facies b and c show a reversed bell shape  
205 behavior, with the minimum value recorded at  $-1^{\circ}\text{C}$  and an absolute maximum at  $-3^{\circ}\text{C}$ . Therefore, from a  
206 thermal point of view, only facies b is different. Moreover, at depths below the level of zero annual amplitude,  
207 this facies occurs only at depths of 34.5m and 90 m with a negligible thickness (2 and 1 m respectively) and at  
208 142.5 m and 205 m where it reaches 3-3.5 m in thickness. Clearly, the thermal influence of this facies is  
209 negligible: indeed, the gradient between 60 and 235 m is approximately the same as that between 60 and 105  
210 m and between 125 and 205 m.

211 According to the model proposed in the Methods, we found the best fitting with the thermal profiles (Figure 5)  
212 using an heat flow of  $70 \text{ mWm}^{-2}$  (Della Vedova et al., 1995) and a thermal diffusivity value equal to the mean



213 between the value obtained for 0°C and -1°C for facies a, which is the more widespread in the borehole. The  
214 linear system (4) was assembled including the detrended data measured at SSB in 2015 ( $T_j = 0$ ), in 2014  
215 ( $T_j = 1$ ) and 2013 ( $T_j = 2$ ), at the 13 depths listed in Section 3.1, resulting in 39 equations. The anomalies of  
216 the GST reconstruction obtained with respect to the reference period between 1880 and 1960 has been  
217 computed using the value of  $\alpha = 0.95$  for the regularization parameter (Figure 6).

218

## 219 5 DISCUSSION

### 220 5.2.1 GST and current air temperatures

221 In cryotic environments, snow cover can influence GST variability both in space and in time (e.g. Zhang, 2005;  
222 Schmidt et al., 2009; Morse et al., 2012; Rodder and Kneisel, 2012; Schmid et al., 2012; Guglielmin et al., 2014).  
223 This is especially the case for alpine areas where topography influences both the re-distribution of the snow by  
224 wind-drift and actual snow cover evolution (e.g. melting date and duration). Nevertheless, GST and air  
225 temperature are well correlated ( $R^2 = 0.8027$ ) and present a very similar pattern over the last 15 years with only  
226 a slight warming (Figure 7). This relatively slight effect of snow at this site is probably due to the high wind  
227 velocities during winter that, on average, prevent buildup of a thick snowpack. Figure 8 illustrates the temporal  
228 variability of snow cover on the GST. In general, the highest ( $>\pm 5^\circ\text{C}$ ) differences between mean daily GST and  
229 mean daily air temperature occur when there are large drops of air temperature during the winter. Sometimes,  
230 large differences occur also when there are large drops of air temperature during the summer where there is  
231 little or no snow cover, because of high solar radiation that heats the ground surface. Correlation is even better  
232 between monthly mean air temperature, mean annual air temperature (MAAT) and mean annual ground  
233 surface temperature (MAGST) ( $R^2 = 0.8712$  for this latter). This agrees with the results of Zhang and Stamnes,  
234 (1998) who found that, in a flat area in northern Alaska, changes in seasonal snow cover had a smaller effect  
235 than MAAT on the ground thermal regime.

### 236 5.2.2. GST Fluctuations between 1950 and today

237 Our reconstruction after the cold GST anomaly, between 1906 and 1941 AD, shows a slightly positive peak  
238 ( $0.15^\circ\text{C}$ ) in 1930 and afterwards a very unstable period with a first sharp decrease of temperature until 1989 ( $-$   
239  $0.8^\circ\text{C}$ ) and a second even sharper increase, reaching in 2011 the uppermost GST anomaly value of the last 500  
240 years ( $0.96^\circ\text{C}$ ).

241 On a regional scale, the Stelvio data can be compared with the MAAT obtained for the Alps by Christiansen and  
242 Ljungqvist, (2011) (Figure 6) and Trachsel et al., (2010). The maximum of the slight temperature increase during  
243 the first half of the XX century in the Stelvio data (1930) falls exactly in the middle of the relative warming  
244 period between 1925 and 1935 in the Alps found by Trachsel et al., (2010) and is in good agreement with the  
245 date (1928) indicated by Christiansen and Ljungqvist, (2011). Later, the sharp GST anomaly decrease was  
246 delayed in the Stelvio data (1989) with respect to 1950-1965 period found by Trachsel et al., (2010) and 1965-





1975 period found by Christiansen and Ljungqvist, (2011). Finally, the most recent increase of temperature culminated in the Alps in 1994 (Christiansen and Ljungqvist, 2011) while in the Stelvio data at 2011.

### 5.2.3 The Little Ice Age (LIA)

The Stelvio reconstruction shows a long period of negative anomaly between 1560 and 1860 AD with the colder conditions ( $< -2$ \*S.D.) between 1683 and 1784 AD with a peak of  $-1.5^{\circ}\text{C}$  around 1730 AD. This period of negative anomaly falls within this well-known cooling period (LIA). It is recognized in several kinds of proxy data although there are differences both in magnitude and in timing across the world. According to Neukom et al., (2014), synchronous cold temperature anomalies occurred at decadal scale in both hemispheres between 1594 and 1677 AD. They also found two phases of extreme cold temperature in the Northern Hemisphere with the first between 1570 and 1720 AD and the second between 1810 and 1855. Syntheses of the LIA in the European Alps have been presented by Trachsel et al., (2012) and Christiansen and Ljungqvist, (2011). Considering the common colder periods in these two Alpine syntheses, the LIA has three main negative peaks at 1570-1600; 1685-1700 and 1790-1820 AD.

The LIA period has been also characterized by a widespread worldwide glacier advance, although the comparison between glacial evidences and temperature fluctuations are problematic because glaciers respond with different time scales (mainly depending on their size) and reflect also the precipitation regime, which is even more variable in space and time. According to Holzhauser et al., (2005), the LIA advance of the main Swiss Glaciers has three peaks around respectively 1350, 1640 and 1820-50 AD with the two later phases almost synchronous also in the Eastern Alps (Nicolussi and Patzelt, 2000).

Close to the location of the Stelvio borehole, the maximum LIA advance was diachronous. Nearby glaciers show a maximum LIA advance in 1580 AD (Trafoi Valley glacier; Cardassi, 1995), around 1770 AD (Solda Glacier; Arzuffi and Pelfini, 2001) and in 1600 AD (La Mare Glacier; Carturan et al., 2014).

The borehole area was presumably overcapped by the Vedretta Piana Glacier until 1868. Due to the geomorphological position (on a watershed divide) the possible glacier should have been very thin and possibly cold based, as already stressed by Guglielmin et al., (2001). On the other hand, considering figure 6, the glacier should have been present in the borehole area with a buffering effect only between 1711 and 1834 AD, with a peak at 1760, when the difference between the GST anomaly and the MAAT anomaly was maximum. This peak is pretty similar to the peak of the LIA in the Solda Glacier (1770 AD) but not to the peak in the Trafoi glacier (1580 AD); this could be related to Vedretta Piana having a more similar glacier size and aspect (NE-N) to the Solda Glacier than to the Trafoi Glacier, although this latter is the closest to the Vedretta Piana.

### 5.2.4 Other permafrost borehole temperature reconstructions

Several deep Alaskan boreholes have been used to demonstrate the XX century warming (e.g. Lachenbruch and Marshall, 1986; Lachenbruch et al., 1988) but only a few studies in Europe illustrate GST reconstructions that span a time period greater than 100-150 years (e.g. Isaksen et al., 2001, Guglielmin, 2004). In North America, only Chouinard et al., (2013) shows GST pattern of the last 300 years in the context of the permafrost of



282 Northern Quebec. There, after the LIA (1500-1800 AD), it was found an almost constant and marked warming of  
283 ca 1.4 °C until 1940, followed by a cooling episode ( $\approx 0.4$  °C) which lasted 40–50 yr, and finally a sharp  $\approx 1.7$  °C  
284 warming over the past 15 yr.

285 There is a some similarity between the Stelvio reconstruction and the pattern of Canadian permafrost GST  
286 reported by Chouinard et al., (2013) after the LIA. Indeed, also in our site there was an almost simultaneous but  
287 greater cooling (0.9°C) in the period between 1941 and 1989, followed by a sharp warming of ca 1.7°C. On the  
288 other hand, GST reconstructions can be obtained with different models and it is interesting to compare our  
289 data with, for example, the PMIP3/CMIP5 simulations that include the effect of aerosol forcing by Garcia-Garcia  
290 et al., (2016): there, in the last 500 years, the GST shows a cold anomaly (LIA) between 1582 and 1840, with the  
291 most negative peaks between 1798 and 1840, slightly delayed with respect to our data.

## 292 5 CONCLUSIONS

293 The general climatic pattern of the last 500 years recorded by this mountain permafrost borehole is similar to  
294 the majority of other studies in the European Alps and Central Europe. The main difference concerns post LIA  
295 events. In fact, the different multidisciplinary proxies considered (see Figure 9) do not indicate cooling between  
296 1940 and 1989, with the exceptions of the shorter and less severe cooling found for the Alps. It is also relevant  
297 to stress that the rapid and abrupt GST warming (more than 0.8°C per decade) recorded between 1990 and  
298 2011 in the Stelvio borehole data is similar to the warming recorded in permafrost in northern Quebec. This  
299 warming trend is of the same magnitude as the increase of MAAT between 1990 and 2000 in Central Europe  
300 (Dobrovlny et al., (2010)), and is approximately double that found for the MAAT in the Alps and for Europe as a  
301 the whole (Luterbacher et al., 2004).

302 The Stelvio borehole ground surface temperature reconstruction also allows one to estimate changes in the  
303 Vedretta Piana glacier. This glacier presumably buried the site of the Stelvio borehole with an ice thickness  
304 sufficient to exert a significant buffering effect upon the ground thermal regime between 1711 and 1834 AD.  
305 This was a time when the difference between the Stelvio GST anomaly and the MAAT anomaly was greatest.

306

## 307 6 REFERENCES

308 Arzuffi, L. and Pelfini, M.: I testimoni dei cambiamenti climatici, *Neve e Valanghe*, 43, 44–53, 2001.

309 Auer, I., Böhm, R., Jurkovic, A., Lipa, W., Orlik, A., Potzmann, R., Schöner, W., Ungersböck, M., Matulla, C., Briffa,  
310 K., Jones, P., Efthymiadis, D., Brunetti, M., Nanni, T., Maugeri, M., Mercalli, L., Mestre, O., Moisselin, J.M.,  
311 Begert, M., Müller-Westmeier, G., Kveton, V., Bochnicek, O., Stastny, P., Lapin, M., Szalai, S., Szentimrey, T.,  
312 Cegnar, T., Dolinar, M., Gajic-Capka, M., Zaninovic, K., Majstorovic, Z and Nieplova, E. : HISTALP-historical  
313 instrumental climatological surface time series of the Greater Alpine Region, *Int. J. Climatol.*, 27, 17–46, 2007.

314 Barbante C., Schwikowski, M., Döring T., Gäggeler H. W., C., Schotterer U., Tobler L., Van de Velde K., Ferrari C.,  
315 Cozzi G., Turetta A., Rosman K., Bolshov, M., Capodaglio G., Boutron, C.: Historical record of European



- 316 emissions of trace elements to the atmosphere since the 1650s from alpine snow/ice cores drilled near Monte  
317 Rosa, Environ. Sci. Technol. 38,15, 4085–4090, 2004.
- 318 Beltrami, H. and Bournon, E.: Ground warming patterns in the northern hemisphere during the last five  
319 centuries, Earth Planet. Sc. Lett., 227, 169–177, 2004.
- 320 Böhm, R., Auer, I., Brunetti, M., Maugeri, M., Nanni, T. and Schöner W.: Regional temperature variability in the  
321 European Alps: 1760-1998 from homogenized instrumental time series, Int. J. Climatol., 21, 1779–1801, 2001.
- 322 Büntgen, U., Frank, D. C., Nievergelt, D. and Esper, J.: Summer temperature variations in the European Alps, A.D.  
323 755–2004, J. Climate, 19, 5606–5623., 2006.
- 324 Cardassi, S.P. Geologia del Quaternario e geomorfologia della Valle di Trafoi. Master's Thesis, University of  
325 Milan, 1995.
- 326 Carslaw, H.S. and Jaeger, J.C.: Conduction of Heat in Solids. Oxford Univ. Press, New York. 510 pp. 1959.
- 327 Carturan, L., Baroni, C., Carton, A., Cazorzi, F., Dalla Fontana, G., Delpero, C., Salvatore, M.C., Seppi, R. and  
328 Zanoner, T.: Reconstructing fluctuations of La Mare Glacier (Eastern Italian Alps) in the Late Holocene: new  
329 evidence for a Little Ice Age maximum around 1600 ad., Geografiska Annaler: Series A, Physical Geography, 96,  
330 287–306, 2014.
- 331 Cermak, V., Balling, N., Della Vedova, B., Lucazeau, F., Pasquale, V., Pellis, G., Schulz, R. and Verdoya, M., Heat-  
332 flow data (Italy). In: Blundell, D., Freeman, R., Mueller, St. (Eds.): A Continent Revealed: The European  
333 Geotraverse Database. Cambridge Univ. Press, Cambridge, pp. 49– 57, 1992.
- 334 Chouinard, C., Fortier, R., and Mareschal J.C.: Recent climate variations in the subarctic inferred from three  
335 borehole temperature profiles in northern Quebec, Canada, Earth and Planetary Science Letters, 263, 355–369,  
336 2007.
- 337 Christiansen, B. and Ljungqvist, F. C.: Reconstruction of the extratropical NH mean temperature over the last  
338 millennium with a method that preserves low-frequency variability, J. Climate, 24, 6013-6034, 2011.
- 339 Clauser C, and Huenges E. :Thermal conductivity of rocks and minerals. In Rock Physics and Phase Relations. A  
340 Handbook of Physical Constants, Ahrens TJ (ed). AGU Reference Shelf 3. American Geophysical Union:  
341 Washington; 105–126, 1995.
- 342 Cook, B.I., Bonan, G.B., Levis, S. and Epstein, H.E.: The thermoinsulation effect of snow cover within a climate  
343 model, Clim. Dyn, 31, 107–124, 2008.
- 344 Corona, C., Guiot, J., Edouard, J.L., Chalié, F., Büntgen, U., Nola, P. and Urbinati, C.: Millennium-long summer  
345 temperature variations in the European Alps as reconstructed from tree rings. Climate of the Past, 6, 379-400,  
346 2010.



- 347 Della Vedova, B., Lucazeau, F., Pasquale, V., Pellis, G., and Verdoya.: M. Heat flow in the tectonic provinces  
348 crossed by the southern segment of the European Geotraverse, *Tectonophysics*, 244 ,57-74, 1995
- 349 Dobrovolný, P., Moberg, A., Brázdil, R., Pfister, C., Glaser, R., Wilson, R., van Engelen, A., Limanówka, D., Kiss,  
350 A., Halíčková, M. Macková, J. Riemann, D. Luterbacher, J. and Böhm R.: Monthly, seasonal and annual  
351 temperature reconstructions for Central Europe derived from documentary evidence and instrumental records  
352 since AD 1500, *Climatic Change*, 101, 69–107, 2010.
- 353 García-García, A., Cuesta-Valero, F. J., Beltrami, H. and Smerdon, J. E.: Simulation of air and ground  
354 temperatures in PMIP3/CMIP5 last millennium simulations: implications for climate reconstructions from  
355 borehole temperature profiles, *Environmental Research Letters*, 11, 044022, 2016
- 356 Golub, G. H., Heath M., and Wahba G.: Generalized Cross-Validation as a Method for Choosing a Good Ridge  
357 Parameter, *Technometrics*, 21 ,2, 215-223, 1979.
- 358 Gruber, S., King, L., Kohl, T., Herz, T., Haeberli, W. and Hoelzle, M.: Interpretation of geothermal profiles  
359 perturbed by topography: the Alpine permafrost boreholes at Stockhorn Plateau, Switzerland, *Permafrost and*  
360 *Periglacial Processes*, 15, 349–357, 2004.
- 361 Guglielmin, M.: Observations on permafrost ground thermal regimes from Antarctica and the Italian Alps, and  
362 their relevance to global climate change, *Global and Planetary Change*, 40, 159–167, 2004.
- 363 Guglielmin, M., Cannone, N., and Dramis, F.: Permafrost-glacial evolution during the Holocene in the Italian  
364 Central Alps, *Permafrost Periglacial Processes*, 12, 111–124, 2001
- 365 Guglielmin, M., Worland, M.R., Baio, F. and Convey, P.: Permafrost and snow monitoring at Rothera Point  
366 (Adelaide Island, Maritime Antarctica): Implications for rock weathering in cryotic conditions, *Geomorphology*,  
367 225, 47–56, 2014.
- 368 Hansen, P.: Rank-Deficient and Discrete Ill-Posed Problems, *Society for Industrial and Applied Mathematics*,  
369 1998.
- 370 Harris, C., Haeberli, W., Vonder Muhl, D. and King, L.: Permafrost monitoring in the high mountains of Europe:  
371 the PACE Project in its global context, *Permafrost and Periglacial Processes*, 12, 3 – 11, 2001.
- 372 Harris, C., Vonder Mühll, D, Isaksen, K., Haeberli, W., Sollid, J.I., King, L., Holmlund, P., Dramis, F., Guglielmin, M.  
373 and Palacios, D.: Warming permafrost in European mountains, *Global and Planetary Change*, 39, 215-225, 2003.
- 374 Hilbich, C., Hauck, C., Hoelzle, M., Scherler, M., Schudel, L., Völksch, I., Vonder Mühll, D. and Mäusbacher, R.:  
375 Monitoring mountain permafrost evolution using electrical resistivity tomography: a 7-year study of seasonal,  
376 annual, and long-term variations at Schilthorn, Swiss Alps, *J. Geophys. Res.*, 113, F01S90. 2008.
- 377 Holzhauser, H., Magny, M. and Zumbühl, H.J.: Glacier and lake-level variations in west-central Europe over the  
378 last 3500 years, *The Holocene*, 15, 6, 789–801, 2005.



- 379 Huang, S., Pollack, H. N. and Shen, P. Y.: Temperature trends over the last five centuries reconstructed from  
380 borehole temperatures, *Nature*, 403, 756–758, 2000.
- 381 IPCC. Summary for policymakers, In *Climate Change 2013: The Physical Science Basis. Contribution of Working*  
382 *Group I to the Fifth Assessment Report of the Intergovernmental Panel on Climate Change*, Stocker, T.F., Qin, D.,  
383 Plattner, G.K., Tignor, M.S.K., Allen, J., Boschung, A., Nauels, Y., Xia, Y., Bex, V., Midgley, P.M., (eds) Cambridge  
384 University Press: Cambridge, UK and New York, NY, 2013.
- 385 Isaksen, K., Vonder Muhll, D., Gubler, H., Kohl, T. and Sollid, J.L.: Ground surface-temperature reconstruction  
386 based on data from a deep borehole in permafrost at Janssonhaugen, Svalbard, *Annals of Glaciology*, 31, 287–  
387 294. 2001.
- 388 Lachenbruch, A.H. and Marshall, B.V.: Changing climate: geothermal evidence from permafrost in the Alaskan  
389 Arctic, *Science* 234, 689– 696, 1986.
- 390 Lachenbruch, A.H., Cladouhos, T.T. and Saltus, R.W.: Permafrost temperature and the changing climate.  
391 “Permafrost”, 5th International Permafrost Conference Proceedings, vol. 3. Tapir Publishers, Trondheim,  
392 Norway, pp. 9–17, 1988.
- 393 Larocque-Tobler, I., Grosjean, M., Heiri, O., Trachsel, M., and Kamenik, C.:Thousand years of climate change  
394 reconstructed from chironomid subfossils preserved in varved lake Silvaplana, Engadine, Switzerland,  
395 *Quaternary Science Reviews*, 29, 1940–1949, 2010.
- 396 Lewis, T. J. and Wang, K.: Influence of terrain on bedrock temperatures, *Palaeogeogr. Palaeoclimatol.*  
397 *Palaeoecol.* 98, 87–100, 1992
- 398 Ling, F. and Zhang, T.J.: Sensitivity of ground thermal regime and surface energy fluxes to tundra snow density in  
399 northern Alaska, *Cold Reg. Sci. Technol.*, 44, 121–130, 2006.
- 400 Liu J. and Zhang T.: Fundamental solution method for reconstructing past climate change from borehole  
401 temperature gradients, *Cold Regions Science and Technology*, 102, 32-40, 2014.
- 402 Luterbacher, J., Dietrich, D., Xoplaki, E., Grosjean, M., and Wanner, H.: European seasonal and annual  
403 temperature variability, trends, and extremes since 1500, *Science*, 303, 1499–1503,2004.
- 404 Morse, P.D., Burn, C.R. and Kokelj, S.V.: Influence of snow on near-surface ground temperatures in upland and  
405 alluvial environments of the outer Mackenzie Delta, N.W.T. *Can. J. Earth Sci.*, 49, 895–913, 2012.
- 406 Neukom, R., Gergis, J., Karoly, D.J., Wanner, H., Curran, M., Elbert, J., González-Rouco, F., Linsley, B.K., Moy, A.  
407 D., Mundo, I., Raible, C. C., Steig, E. J., van Ommen, T., Vance, T., Villalba, R., Zinke, J. and Frank, D.: Inter-  
408 hemispheric temperature variability over the past millennium, *Nature Climate Change*, 4, 362–367, 2014.
- 409 Nicolussi, K. and Patzelt, G.: Discovery of early Holocene wood and peat on the forefield of the Pasterze Glacier,  
410 Eastern Alps, Austria, *The Holocene*, 10, 191–199, 2000.



411 Rodder, T. and Kneisel, C.: Influence of snow cover and grain size on the ground thermal regime in the  
412 discontinuous permafrost zone, Swiss Alps. *Geomorphology*, 175-176, 176–189, 2012.

413 Schmid, M.O., Gubler, S., Fiddes, J. and Gruber, S.: Inferring snowpack ripening and melt-out from distributed  
414 measurements of near-surface ground temperatures, *The Cryosphere*, 6, 1127–1139, 2012.

415 Schmidt, S., Weber, B. and Winiger M.: Analyses of seasonal snow disappearance in an alpine valley from micro-  
416 to meso-scale (Loetschental, Switzerland), *Hydrol. Process.*, 23, 1041–1051, 2009.

417 Serra-Capizzano, S.: A note on the antireflective boundary conditions and fast deblurring models. *SIAM Journal*  
418 *on Scientific Computing*, 25-4, 1307–1325, 2004.

419 Trachsel, M., Grosjean, M., Larocque-Tobler, I., Schwikowski, M., Blass, A., Sturm, M.: Quantitative summer  
420 temperature reconstruction derived from a combined biogenic Si and chironomid record from varved sediments  
421 of Lake Silvaplana (south-eastern Swiss Alps) back to AD 1177. *Quaternary Science Reviews*, 29, 2719-2730,  
422 2010.

423 Trachsel, M., Kamenik, C., Grosjean, M., McCarroll, D., Moberg, A., Brázdil, R., Büntgen, U., Dobrovolný, P.,  
424 Esper, J., Frank, D. C., Friedrich, M., Glaser, R., Larocque-Tobler, I., Nicolussi, K. and Riemann D.: Multi-  
425 archive summer temperature reconstruction for the European Alps, AD 1053–1996, *Quaternary Science*  
426 *Reviews*, 46, 66-79, 2012.

427 Zhang, T.: Influence of the seasonal snow cover on the ground thermal regime: An overview, *Rev. Geophys.*, 43,  
428 RG4002, 2005.

429 Zhang, T. and Stamnes K.: Impact of climatic factors on the active layer and permafrost at Barrow, Alaska,  
430 *Permafrost Periglacial Processes*, 9, 229–246,1998.

431

## 432 **7 ACKNOWLEDGEMENTS**

433 The SSB borehole was drilled and equipped thanks to the Project “Share Stelvio” managed by EvK2-CNR and  
434 funded by Regione Lombardia. The research was also funded through the PRIN 2008 project “Permafrost e  
435 piccoli ghiacciai alpini come elementi chiave della gestione delle risorse idriche in relazione al Cambiamento  
436 Climatico” leaded by Prof. C. Smiraglia. Special thanks to the Stelvio National Park, SIFAS and Umberto Capitani  
437 for the permissions and the logistical support. We want also to thank you very much Prof. Hugh M. French for  
438 the revision and the English editing of the manuscript.

439

440

441



## 442 **Figure and Table Captions**

443 Figure 1. Study area: (a) Location of the study area with the surrounding glaciers and the reconstructed glaciers  
444 limits of the area (VPG = Vedretta Piana Glacier; TFG = Trafoi Glacier; SG = Solda Glacier; LMG = La Mare Glacier;  
445 PACE = Pace Borehole; SSB = Share Stelvio Borehole); (b) View of the drilling equipment during the realization of  
446 the SSB borehole in summer 2009.

447 Figure 2. Topography of the SSB site: a) Digital Elevation Model (5 m resolution) of the SSB site and b) SSW-NNE  
448 transect through the Stelvio summit. Horizontal and vertical dimensions as well as thermistor chain position and  
449 depths are plotted to the same scale.

450 Figure 3. Piece-wise constant GST history

451 Figure 4. Share Stelvio Borehole (SSB) Stratigraphy. Legend: (A) facies a (massive dolostone from grey to pinky  
452 grey); (B) facies b (white dolostone); (C) facies c (black stratified limestone); (D) facies d (light brown dolostone).

453 Figure 5. SSB mean annual ground temperature profiles on 2013, 2014 and 2015.

454 Figure 6. Comparison between the anomaly of the mean annual GST reconstructed by SSB borehole and MAAT  
455 anomaly reconstructed for the European Alps by Christiansen and Ljungqvist (2011) (data available online at:  
456 <https://www.ncdc.noaa.gov/paleo/study/12355>) both respect the same reference period (1880-1960).

457 Figure 7. Trend of monthly mean of GST and Air temperature at SSB since 1998. The red and blue dashes lines  
458 are respectively the linear regression of the GST and Air temperature.

459 Figure 8. Effect of the snow cover at SSB. The winter 2010/11 is representative of the average conditions of the  
460 snow cover at SSB while the following season 2011/12 was the snowiest of the whole monitoring period. The  
461 difference between the daily mean GST and air temperature ( $\Delta\text{GST}_{\text{air}}$ ) shows the greater values during the  
462 greater drop of the air temperature (green line) during the winter due to the insulating effect of the snow cover  
463 whereas the few episodes of high  $\Delta\text{GST}_{\text{air}}$  in the summer are may due to the solar radiation that warms up the  
464 ground surface.

465 Figure 9. Main climatic events enhanced by anomalies of MAAT through different proxy in all Europe: A,  
466 (rielaborated from Luterbacher et al., 2004); Central Europe: B, (rielaborated from Dobrovolný et al., 2010; Alps:  
467 C, (rielaborated from the same data of Figure 5, Christiansen and Ljungqvist, 2011) and SSB: D, (this paper).

468 Table 1. Thermal gradients ( $^{\circ}\text{Cm}^{-1}$ ) on 2013; 2014 and 2015 in the different depth intervals of the profile below  
469 the zero-annual amplitude that is approximately at 20 m of depth.

470 Table 2. Thermal properties of the three different facies occurred in SSB borehole measured in the Laboratory  
471 at three different steps of temperature (0; -1 and  $-2^{\circ}\text{C}$ ).

472



473

474

475

476 Table 1

	20-60 m (°Cm <sup>-1</sup> )	60-105 m (°Cm <sup>-1</sup> )	105-125 m (°Cm <sup>-1</sup> )	125-205 m (°Cm <sup>-1</sup> )	205-215 m (°Cm <sup>-1</sup> )	215-235 m (°Cm <sup>-1</sup> )	60-235 m (°Cm <sup>-1</sup> )
2013	0,0088	-0,0072	-0,0048	-0,0075	-0,0128	-0,0058	-0,0072
2014			-0,0046	-0,0074	-0,0128	-0,0056	
2015	0,0086	-0,0077	-0,0045	-0,0073	-0,0128	-0,0055	-0,0072

477

478

479 Table 2

	Density (gcm <sup>-3</sup> )	Diffusivity (10 <sup>-6</sup> m <sup>2</sup> s <sup>-1</sup> )	Heat capacity (Jg <sup>-1</sup> K <sup>-1</sup> )	Conductivity (WmK <sup>-1</sup> )
<b>Facies a</b>	2.714			
0°C		2,171	0,759	4,474
-1°C		2,105	0,763	4,360
-3°C		2,081	0,765	4,320
<b>Facies b</b>	2.827			
0°C		2,798	0,786	6,216
-1°C		2,762	0,791	6,177
-3°C		2,763	0,794	6,201
<b>Facies c</b>	2.696			
0°C		1,968	0,762	4,044
-1°C		1,892	0,767	3,912
-3°C		1,936	0,769	4,015

480

481

482

483

484

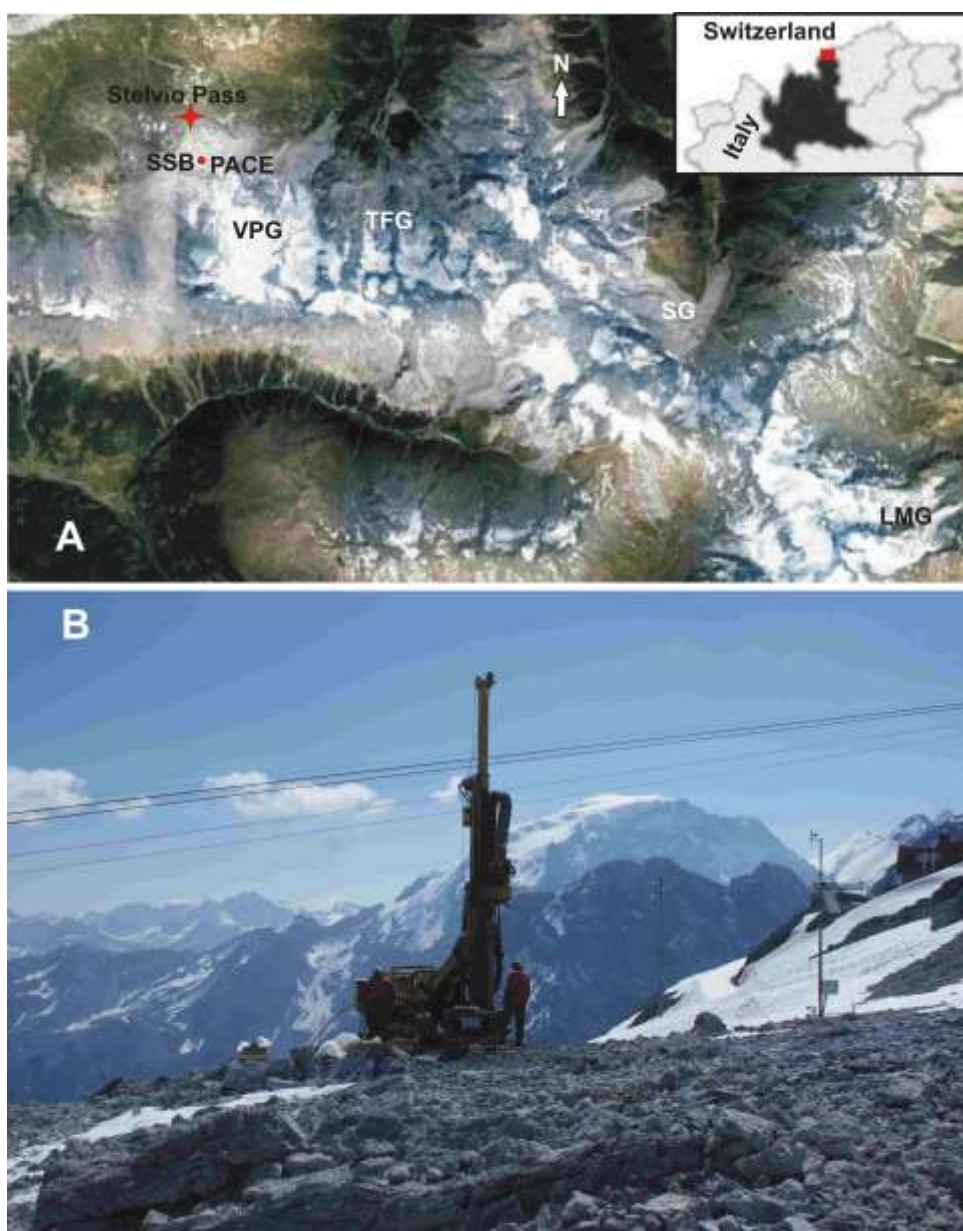
485





486

487 Figure 1

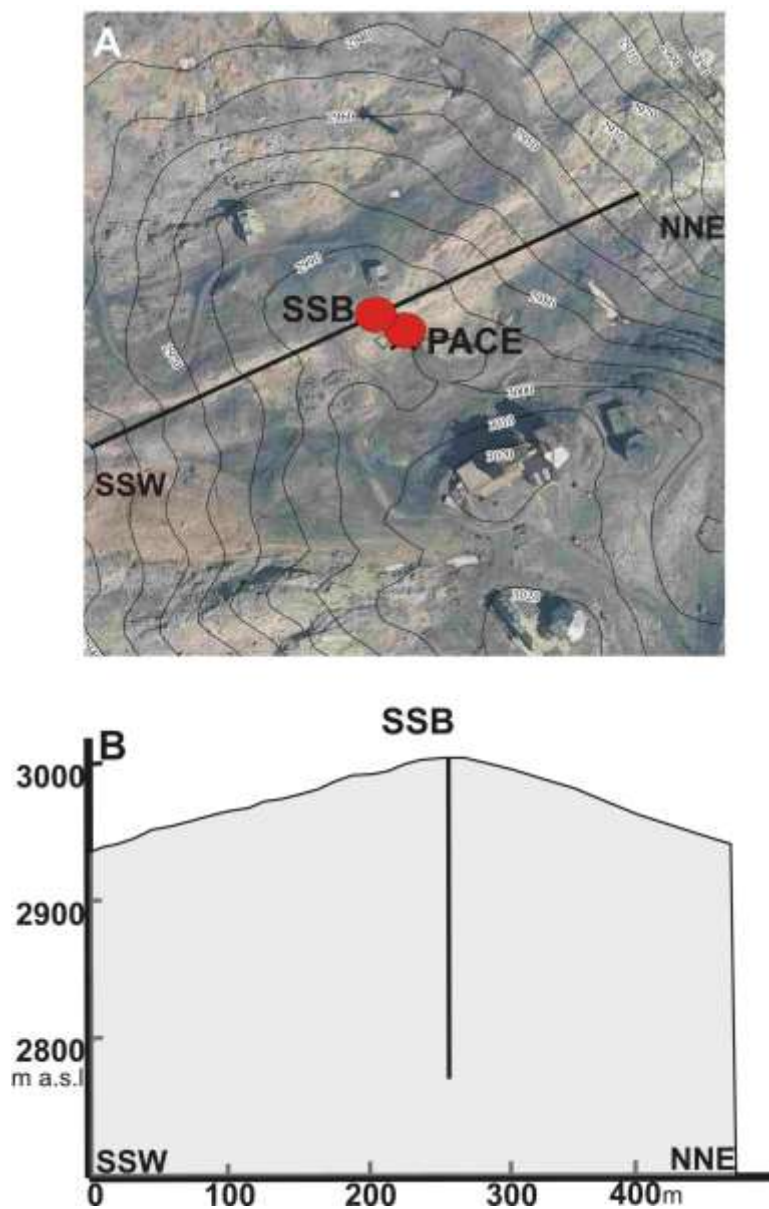


488

489



490 Figure 2

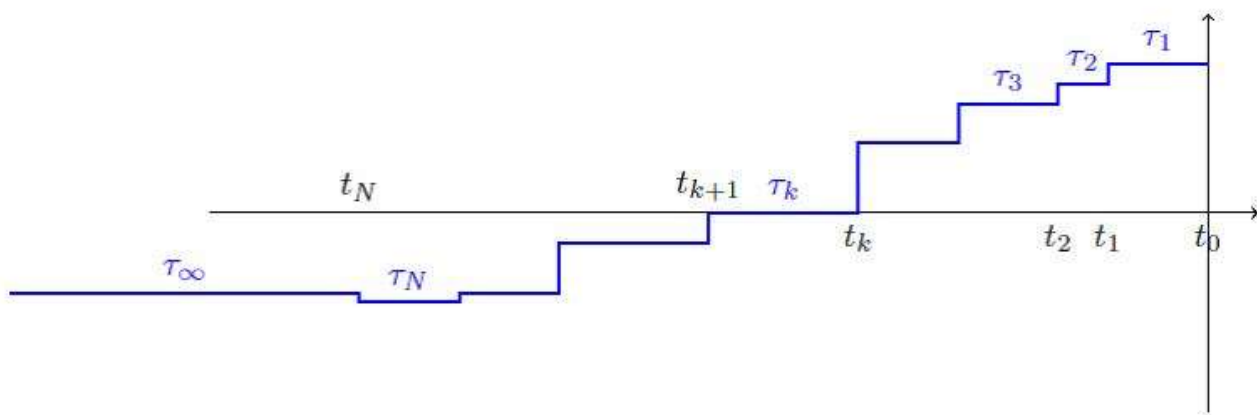


491

492



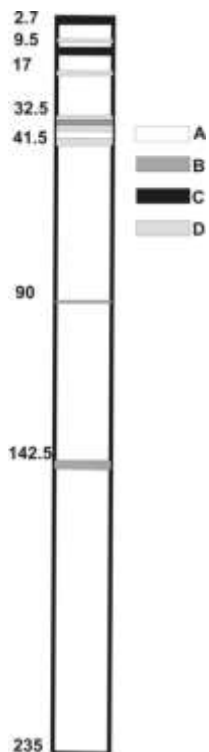
493 Figure 3



494

495

496 Figure 4

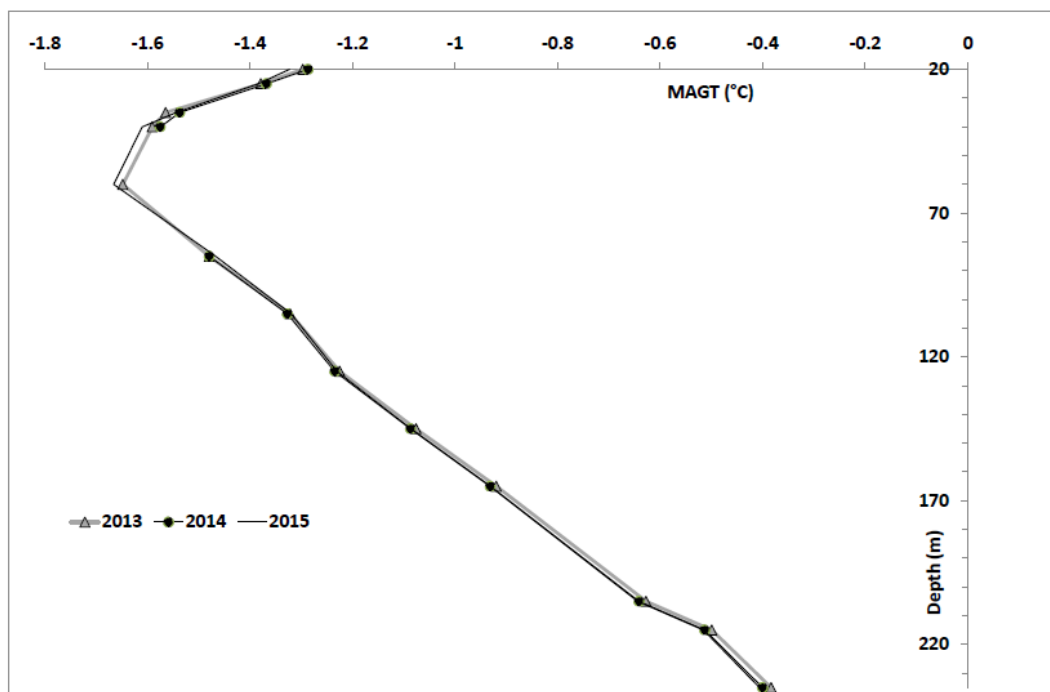


497

498



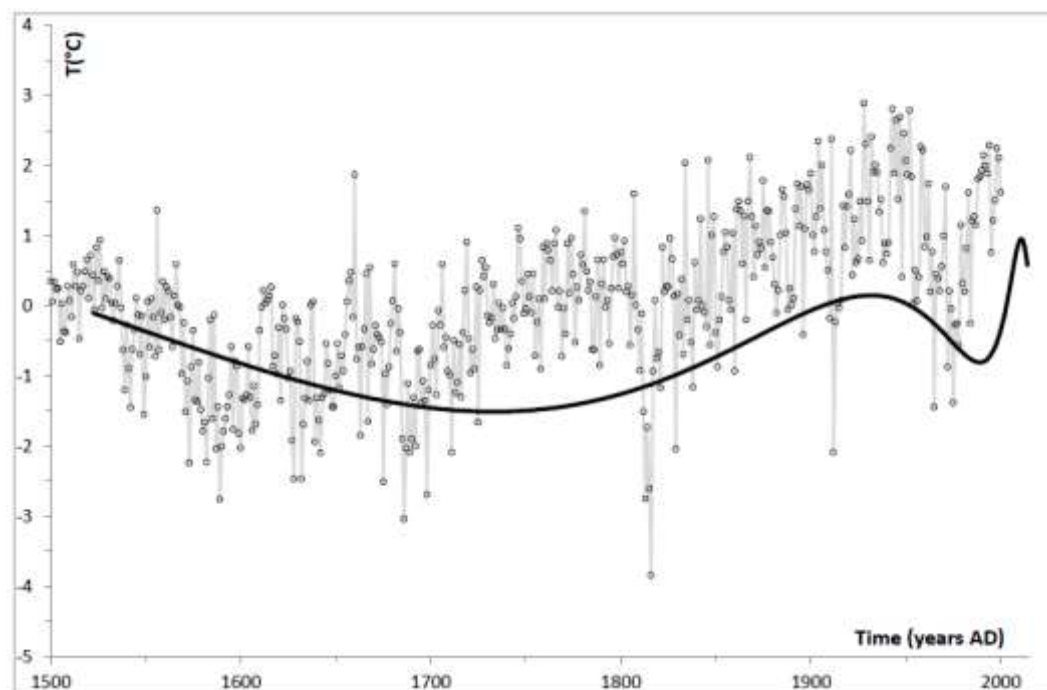
499 Figure 5



500

501

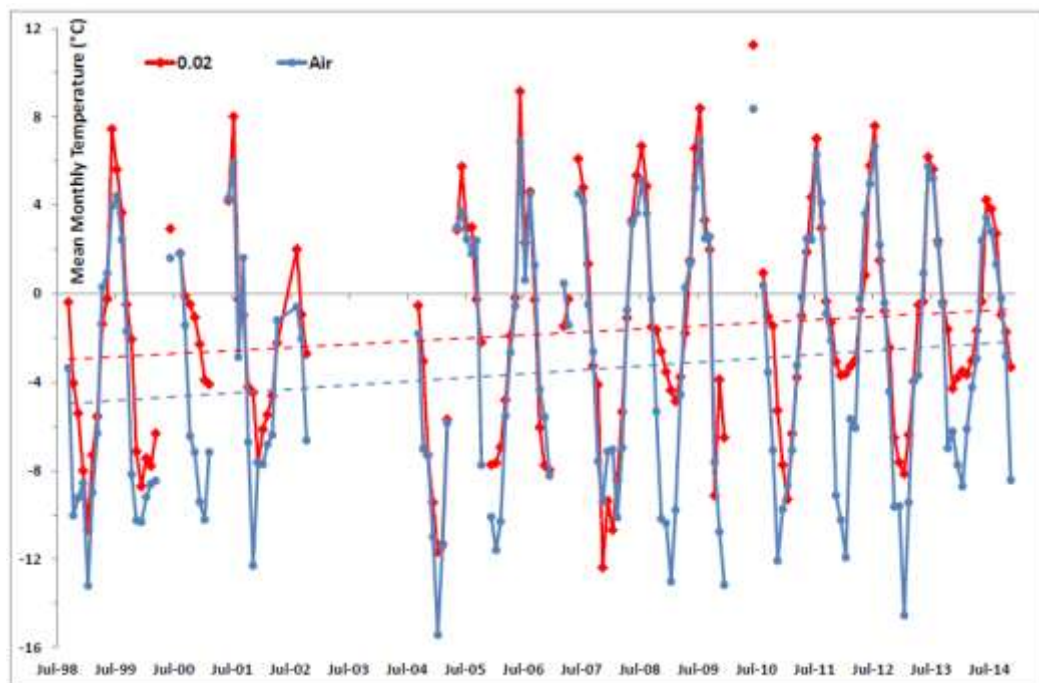
502 Figure 6



503

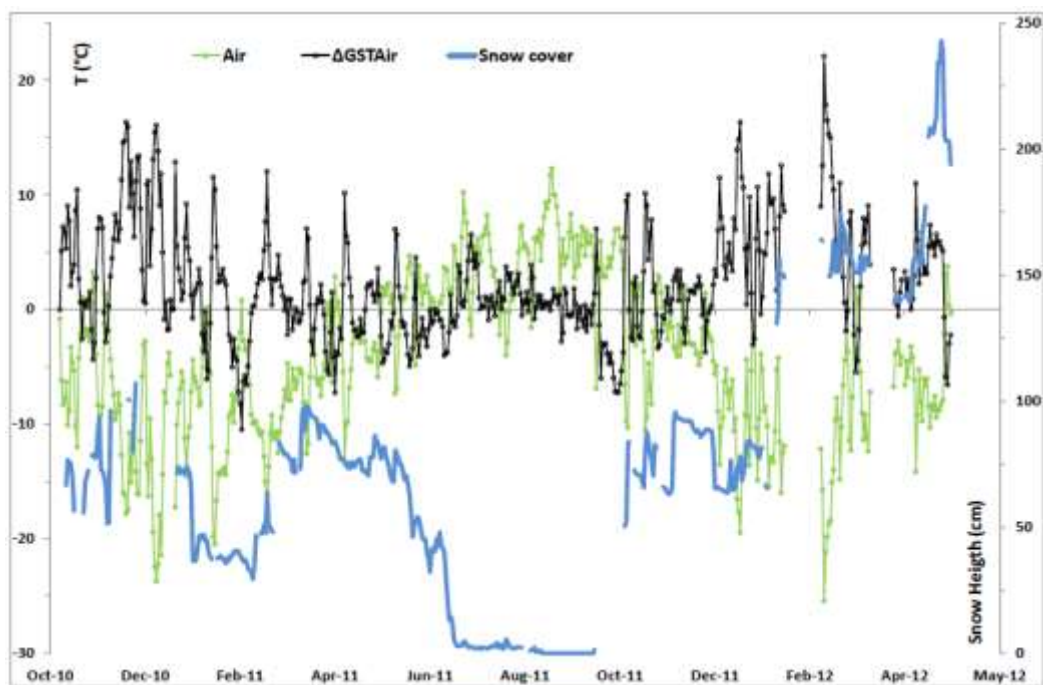


504 Figure 7



505

506 Figure 8



507

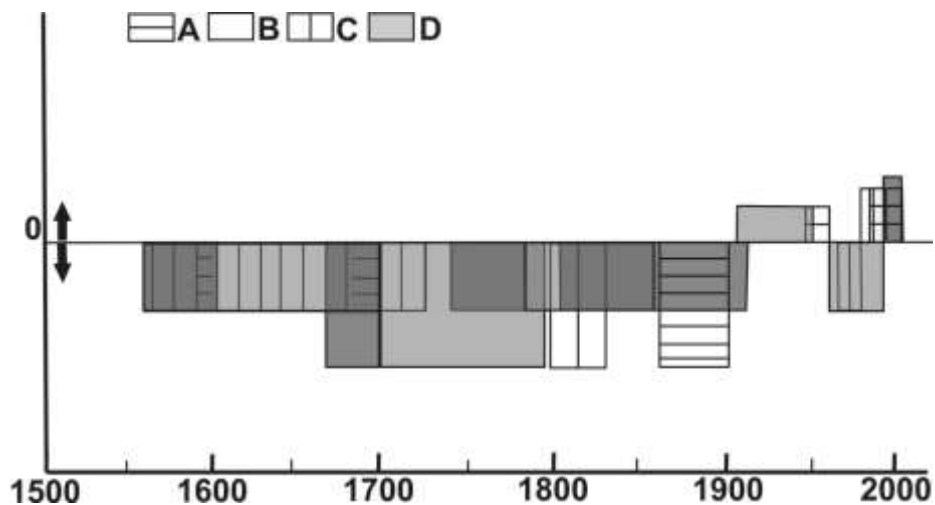
508



509 Figure 9

510

511



512

513

514